Polymer 51 (2010) 316–327

Contents lists available at ScienceDirect

Polymer

journal homepage: www.elsevier.com/locate/polymer

Frozen-in birefringence and anisotropic shrinkage in optical moldings: I. Theory and simulation scheme

Avraam I. Isayev*, Tsui-Hsun Lin

Institute of Polymer Engineering, The University of Akron, Akron, OH 44325-0301, USA

ARTICLE INFO

Article history:
Received 20 June 2009
Received in revised form
30 October 2009
Accepted 2 November 2009
Available online 10 November 2009

Keywords:
Numerical simulation
Injection molding
Flow birefringence

ABSTRACT

An unconditionally stable upwinding scheme was proposed to improve the efficiency of the viscoelastic simulation in molding of optical products using a CV/FEM/FDM technique. A significant computation time saving was achieved due to an elimination of subdivision of the time step as required in the conventional numerical scheme. The approach was applied to simulate the flow-induced birefringence and anisotropic shrinkage in disk moldings using a nonlinear viscoelastic constitutive equation, orientation functions and equation of state. The two-dimensional triangular finite element meshes were used in the disk cavity and the one-dimensional tubular elements were utilized in the delivery system. Good agreement was shown between the simulated pressure traces and flow birefringence in the molding using the unconditionally stable upwinding scheme of the present study and the conventional numerical scheme of the earlier study. In addition, an algorithm for simulation of the thermal stresses and birefringence in moldings using linear viscoelastic and photoviscoelastic constitutive equations was presented by combining constrained and free quenching approaches. The proposed numerical scheme for viscoelastic simulation of injection molding is more suitable for future commercial applications.

1. Introduction

The manufacturing of precision plastic optical parts such as lenses, disk substrates, light guide plates (LGPs) and other optical components by injection and injection/compression molding processes is an important industrial technology. Over the years, a number of attempts on modeling the residual stresses and molecular orientation in injection molding of amorphous polymers have been made by various researchers. Recent paper [1] provides a brief overview of studies devoted to the subject matter and efforts in simulation of optical retardation in disk substrates made of amorphous polymers. A new approach was also proposed for the simulation of anisotropic shrinkage in moldings of amorphous polymers [2]. Recently, a review of various approaches available to calculate anisotropic shrinkage in moldings was made [3].

LGPs are used in backlight system comprising of a light source, an LGP and various layers of reflective, diffusive and optical prism films. In this system, the light rays from the source are directed into the side of the LGP, sometimes both sides, and are guided inside the plate based on the total internal reflection. The rays are reflected and refracted by micro patterns at the bottom of the LGP, which could be an array of ink printed white spots [4] or V-groove microstructures [5,6]. The major concern in the manufacturing of LGPs is the light transmission, termed luminance, because plastic LGP needs to deliver the light from its edges to the front surface with the highest possible efficiency. It was recently found that the processing conditions in injection molding have a strong effect on the luminance of V-groove LGPs [7]. In particular, the luminance of LGPs made of optical grade polycarbonates was measured and found to be affected by the depth of melt filling of the grooves and frozen-in birefringence. Imperfections in filling of V-grooves are influenced by local pressure and temperature histories. Measurements of the depth of melt filling were carried out at different locations in moldings obtained at various processing conditions. The influence of molding conditions on filling of V-grooves and luminance performance of LGPs was elucidated. Also, a series of experiments were performed to investigate the effects of cavity conditions on transcription molding of micro-scale prisms made of PMMA [8]. It was found that melt filling of the V-grooves can be affected by the pitch, direction of groove layout, direction of melt flow propagation and cavity pressure during melt filling stage. It was concluded that the transcription during the melt filling stage dominates the entire transcription process. Typically, an ideal layout of V-grooves can be optimized by an optical simulation [9,10] that may lead to an optimal luminance of LGPs. However, it should be noted that the luminance is also related to the frozen-in

* Corresponding author.
E-mail address: aisayev@uakron.edu (A.I. Isayev).

0032-3861/$ – see front matter © 2009 Elsevier Ltd. All rights reserved.
doi:10.1016/j.polymer.2009.11.006

molecular orientation (birefringenc) in LGPs [7]. Thus, there is a real need to simulate the frozen-in birefringence in optical products.

Part I of the present study describes a numerical simulation of one- and two-dimensional flow using a control volume/finite element/finite difference method (CV/FEM/FDM) in injection molding process of an optical disk including the filling, packing and cooling stages. The compressible Leonov model [11] is used to calculate the flow stresses and the flow birefringence related to the flow stresses through the empirical linear stress-optical rule [12]. In carrying out the present viscoelastic simulations, an unconditionally stable upwinding scheme [13] is used to remedy the limitations on small time step requirement of the previous calculations [1]. The linear viscoelasticity and photoviscoelasticity together with the first order rate equation for the volume relaxation [14,15] are employed to calculate the thermal stresses and the thermal birefringence using a combination of constrained and free quenching approaches. The orientation function, equation of state and elastic recovery are used to simulate anisotropic shrinkage. In Part 2 the predicted birefringence and anisotropic shrinkages in LGP moldings will be compared with the experimental results obtained at different processing conditions.

2. Theory and governing equations

2.1. Residual flow stresses and birefringence

Mold filling during the injection molding process is comprised of three stages: filling, packing and cooling. Flow stresses and birefringence are arised as a result of cavity filling and packing stages. Due to the viscoelastic nature of a polymer melt and fast cooling the flow stresses and birefringence do not completely relax and remain residual in moldings. The momentum equations, in the absence of inertia and body forces, and the mass balance equation are:

$$\frac{\partial \sigma_{xx}}{\partial x}+\frac{\partial \sigma_{xz}}{\partial z}=0 \tag{1}$$

$$\frac{\partial \sigma_{yy}}{\partial y}+\frac{\partial \sigma_{yz}}{\partial z}=0 \tag{2}$$

$$\frac{\partial \rho}{\partial t}+\frac{\partial}{\partial x}(\rho v_x)+\frac{\partial}{\partial y}(\rho v_y)=0 \tag{3}$$

where x and y are planar directions and z is the gapwise direction, σ_{ij} represents the total stress, v_x and v_y are velocity components in the x and y directions, respectively.

In a nonisothermal problem, the momentum and mass balance equations are coupled with the energy equation:

$$\rho C_P\left(\frac{\partial T}{\partial t}+v_x\frac{\partial T}{\partial x}+v_y\frac{\partial T}{\partial y}\right)=\frac{\partial}{\partial z}\left(\kappa\frac{\partial T}{\partial z}\right)+\Phi \tag{4}$$

where C_P, $\kappa$and Φ are the specific heat, thermal conductivity and the dissipation function, respectively. The dissipation function is given as [16]

$$\Phi=2\eta_0 s\cdot tre^2+\sum_k\frac{\eta_k}{2\theta_k^2}\left[\frac{I_1(I_2-I_1)}{3}+tr\mathbf{C}_k^2-3\right] \tag{5}$$

where

$$e=\frac{1}{2}\left(\nabla\underline{v}+\nabla\underline{v}^T\right) \tag{6}$$

is the deformation rate tensor and $\boldsymbol{C}_k$ is the elastic strain tensor.

By employing the Leonov constitutive model, the stress tensor can be related to the velocity gradient tensor as follows [11]:

$$\sigma=-P\underline{\delta}+\eta_0 s\left(\nabla\underline{v}+\nabla\underline{v}^T\right)+\sum_k\frac{\eta_k}{\theta_k}\boldsymbol{C}_k \tag{7}$$

with governing equation for $\boldsymbol{C}_k$ being

$$\mathbf{C}_k^{\nabla}+\frac{1}{2\theta_k}\left[\mathbf{C}_k^2+\frac{1}{3}\left(II_C^k-I_C^k\right)\mathbf{C}_k-\mathbf{I}\right]=0 \tag{8}$$

where P is the pressure, s is a rheological parameter lying between zero and one, and η_k and θ_k are, respectively, the shear viscosity and relaxation time of the kth mode, and $\mathbf{C}_k^{\nabla}$ is the Jaumann derivative of the elastic strain tensor, $\boldsymbol{I}$ is the identity tensor and I_C^k and II_C^k are the first and the second invariant of the elastic strain tensor, $\boldsymbol{C}_k$. The Eq. (8) can be expanded as follows:

$$\frac{DC_{xx,k}}{Dt}-2C_{xz,k}\frac{\partial v_x}{\partial z}+\frac{1}{2\theta_k}\left(C_{xx,k}^2+C_{xz,k}^2-1\right)=0 \tag{9a}$$

$$\frac{DC_{yy,k}}{Dt}-2C_{yz,k}\frac{\partial v_y}{\partial z}+\frac{1}{2\theta_k}\left(C_{yy,k}^2+C_{yz,k}^2-1\right)=0 \tag{9b}$$

$$\frac{DC_{zz,k}}{Dt}+\frac{1}{2\theta_k}\left(C_{xz,k}^2+C_{yz,k}^2+C_{zz,k}^2-1\right)=0 \tag{9c}$$

$$\frac{DC_{xz,k}}{Dt}-C_{zz,k}\frac{\partial v_x}{\partial z}+\frac{1}{2\theta_k}\left(C_{xx,k}C_{xz,k}+C_{zz,k}C_{xz,k}\right)=0 \tag{9d}$$

$$\frac{DC_{yz,k}}{Dt}-C_{zz,k}\frac{\partial v_y}{\partial z}+\frac{1}{2\theta_k}\left(C_{yy,k}C_{yz,k}+C_{zz,k}C_{yz,k}\right)=0 \tag{9e}$$

$$\det|C_k|=C_{xx,k}C_{yy,k}C_{zz,k}-C_{xz,k}^2C_{yy,k}-C_{yz,k}^2C_{xx,k}=1 \tag{9f}$$

where $\frac{DC_{ij,k}}{Dt}$ is the substantial derivative of $\boldsymbol{C}_k$ with respect to time:

$$\frac{D\mathbf{C}_k}{Dt}=\frac{\partial\mathbf{C}_k}{\partial t}+v_x\frac{\partial\mathbf{C}_k}{\partial x}+v_y\frac{\partial\mathbf{C}_k}{\partial y} \tag{10}$$

The boundary conditions on velocity, pressure, flow rate and temperature are as follows.

$$v_x=v_y=0, \text{at } z=b \tag{11}$$

$$\frac{\partial v_x}{\partial z}=\frac{\partial v_y}{\partial z}=0 \text{ at } z=0 \tag{12}$$

In the filling stage, pressure at the melt front is assumed to be zero and the flow rate, Q, is specified at the nozzle or sprue entrance.

$$P=0 \text{ at the melt front} \tag{13}$$

$$Q=Q_0 \text{ at the entrance} \tag{14}$$

In the packing stage, the pressure at the nozzle or entrance is assigned according to the applied packing pressure and the flow rate is solved.

$$p=p_{\text{packing}} \text{ at the entrance} \tag{15}$$

To calculate the temperature field, a constant wall (mold) temperature, T_w, and the symmetry along the centerline is assumed:

$$T=T_w \text{ at } z=b \tag{16}$$

$$\frac{\partial T}{\partial z}=0 \text{ at } z=0 \tag{17}$$

In addition, the temperature-dependent viscosity and relaxation time are given by the shift factor, a_T, such as

$$\eta_k(T) = \eta_k(T_r)\frac{a_T}{a_{Tr}} \tag{18}$$

$$\theta_k(T) = \theta_k(T_r)\frac{a_T}{a_{Tr}} \tag{19}$$

where a_T is the shift factor at the temperature T described by the WLF equation:

$$\log a_T = \frac{-C_1(T-T_r)}{C_2+T-T_r} \tag{20}$$

with T_r being the reference temperature. C_1 and C_2 are constants that are obtained by curve fitting of temperature shift factor from viscosity curves measured at different temperatures.

By substituting Eq. (7) into the Eqs. (1) and (2) and integrating the results with respect to z and using the symmetric boundary conditions, Eq. (11), the velocity gradients in the absence of normal forces become:

$$\frac{\partial v_x}{\partial z} = \frac{\partial P}{\partial x}\frac{z}{\eta_x} \tag{21}$$

$$\frac{\partial v_y}{\partial z} = \frac{\partial P}{\partial y}\frac{z}{\eta_y} \tag{22}$$

where:

$$\eta_x = \eta_0 s + \frac{1}{\dfrac{\partial v_x}{\partial z}}\sum_k \frac{\eta_k}{\theta_k}C_{xz,k} \tag{23}$$

$$\eta_y = \eta_0 s + \frac{1}{\dfrac{\partial v_y}{\partial z}}\sum_k \frac{\eta_k}{\theta_k}C_{yz,k} \tag{24}$$

Integration of Eqs. (21) and (22) using Eq. (11), leads to:

$$v_x = -\frac{\partial P}{\partial x}\int_z^h \frac{z'}{\eta_x}\mathrm{d}z' \tag{25}$$

$$v_y = -\frac{\partial P}{\partial y}\int_z^h \frac{z'}{\eta_y}\mathrm{d}z' \tag{26}$$

With substitution of Eqs. (25) and (26) into Eq. (3), the governing equation for pressure becomes:

$$G\frac{\partial P}{\partial t} + H - \frac{\partial}{\partial x}\left(S_x\frac{\partial P}{\partial x}\right) - \frac{\partial}{\partial y}\left(S_y\frac{\partial P}{\partial y}\right) = 0 \tag{27}$$

where:

$$G = \int_0^h \left(\frac{\partial \rho}{\partial P}\right)\mathrm{d}z \tag{28}$$

$$H = \int_0^h \left(\frac{\partial \rho}{\partial T}\right)\left(\frac{\partial T}{\partial t}\right)\mathrm{d}z \tag{29}$$

$$S_x = \int_0^h \left(z\int_0^z \rho\,\mathrm{d}z'\right)\frac{\mathrm{d}z}{\eta_x} \tag{30}$$

$$S_y = \int_0^h \left(z\int_0^z \rho\,\mathrm{d}z'\right)\frac{\mathrm{d}z}{\eta_y} \tag{31}$$

For one-dimensional flow, Eq. (27) reduces to

$$G\frac{\partial P}{\partial t} + H - \frac{\partial}{\partial x}\left(S_x\frac{\partial P}{\partial x}\right) = 0 \tag{32}$$

Eqs. (27) and (32) are the classical Hele-Shaw equations that needs to be solved by numerical methods, as given in Appendix A.

Once the pressures and elastic strain tensor components at calculated nodes are converged, the stress components are calculated according to Eq. (7) at each time step. Then, the flow-induced birefringence components are evaluated by applying the stress-optical rule [12]:

$$\begin{aligned}\Delta n_{xz}^{\mathrm{flow}} &= C_\sigma\sqrt{(\sigma_{xx}-\sigma_{zz})^2+4\sigma_{xz}^2}\\ \Delta n_{yz}^{\mathrm{flow}} &= C_\sigma\sqrt{(\sigma_{yy}-\sigma_{zz})^2+4\sigma_{yz}^2}\\ \Delta n_{xy}^{\mathrm{flow}} &= C_\sigma(\sigma_{xx}-\sigma_{yy})\end{aligned} \tag{33}$$

where the C_σ is the stress-optical coefficient of polymer in the melt state.

2.2. Residual thermal stresses and birefringence

2.2.1. General

The thermally-induced stresses and birefringence are caused by the non-equilibrium density or contraction and the viscoelastic behavior of polymers during an inhomogeneous rapid cooling till the polymer solidifies. The flow- and thermally-induced birefringence is essentially coupled during injection molding process. The viscoelastic constitutive equation, Eqs. (7) and (8), used to describe flow behavior is no longer valid to describe the formation of stresses in solid state. Since polymeric materials during cooling experiences small strains due the temperature decrease below glass transition temperature, a linear viscoelastic and photoviscoelastic constitutive equations are used to evaluate the evolution of the thermal stresses and birefringence. However, in the present study, in contrast to earlier study based on free quenching [1], a combination of constrained and free quenching conditions during molding is employed.

For the case of the linear photoviscoelastic materials, Dill [17] considered the refraction index tensor n_{ij} to be a functional of the strain (or stress) tensor. For the case of small strains, an expansion of the functional in power series and an application of time–temperature superposition lead to the following constitutive equation for linear photoviscoelastic materials under nonisothermal conditions:

$$\begin{aligned} n_{ij} - \frac{n_{kk}}{3}\delta_{ij} &= \int_0^\zeta C_\sigma(\xi-\tau)\frac{\partial}{\partial\tau}\left[\sigma_{ij} - \frac{\sigma_{kk}}{3}\delta_{ij}\right]\mathrm{d}\tau\\ &= \int_0^\zeta C_\varepsilon(\xi-\tau)\frac{\partial}{\partial\tau}\left[\varepsilon_{ij} - \frac{\varepsilon_{kk}}{3}\delta_{ij}\right]\mathrm{d}\tau \end{aligned} \tag{34}$$

with C_σ and C_ε being the stress and strain-optical function dependent on temperature and time. The linear viscoelastic constitutive equation under nonisothermal conditions is [18]:

$$\begin{aligned}\sigma_{ij} = &-P + \int_0^\xi \left\{2G(\xi-\tau)\frac{\partial}{\partial\tau}\left[\varepsilon_{ij} - \frac{1}{3}\varepsilon_{kk}\delta_{ij}\right]\right.\\ &\left. + \delta_{ij}K(\xi-\tau)\frac{\partial}{\partial\tau}[\varepsilon_{kk} - 3\varepsilon_T]\right\}\mathrm{d}\tau\end{aligned} \tag{35}$$

with G and K being the shear and bulk relaxation modulus function dependent on temperature and time and ξ being the reduced time given as

$$\xi = \int_0^t \frac{d\tau}{a_T[T(\tau)]} \tag{36}$$

2.3. Constrained quenching

Constrained quenching is employed when the melt pressure in the cavity is non-zero. In addition, when the temperature is lower than the glass transition temperature ($T \le T_g(P)$), the linear photo-viscoelastic and viscoelastic constitutive equations, Eqs. (34) and (35), are applicable. The pressure dependence of density with the glass transition temperature, T_g (P), given as $T_g = T_g^0 + b_3 P$ is described by the Tait equation [19]:

$$\rho(T,P) = \rho_0(T)\left[1 - \mathbf{C}\ln\left(1 + \frac{P}{B(T)}\right)\right]^{-1} \tag{37}$$

where

$$\rho_0(T) = \rho_0^0\left[1 + \alpha\rho_0^0(T - T_g^0)\right]^{-1} \tag{38}$$

$$B(T) = b_{1l}\exp(-b_{2l}T) \quad \text{if } T > T_g \tag{39}$$

$$B(T) = b_{1s}\exp(-b_{2s}T) \quad \text{if } T \le T_g \tag{40}$$

$$T_g = T_g^0 + b_3 P \tag{41}$$

$$\alpha = \alpha_l \quad \text{if } T > T_g \tag{42}$$

$$\alpha = \alpha_s \quad \text{if } T \le T_g \tag{43}$$

with the T_g^0 being T_g at 1 atm and b_3 being a constant in the Tait equation. Subscripts s and l refers to solid and liquid state, respectively, and α is the thermal expansion coefficient, which is the slope of PVT plot at constant P, and C is a constant.

In case of the constrained quenching, the through thickness thermal stress and lateral strain was determined as [20]:

$$\sigma_{zz} = -p \tag{44}$$

$$\varepsilon_{yy}(z) = \frac{-p}{3K} \tag{45}$$

The lateral strain, ε_{yy}, was calculated at the time of the occurrence of vitrification and maintained until the pressure released or till ejection. At gapwise location where solidification takes place, the lateral stress, σ_{yy}, and the through thickness strain, ε_{zz}, can be calculated as follows. First, if shear stresses are negligible, one considers the linear viscoelastic constitutive equation, Eq. (35), with x and z being the lateral and thickness direction, respectively. Then, Eq. (35) leads to

$$\sigma_{yy} = -P + \int_0^\xi \left\{\frac{2}{3}G(\xi-\tau)\frac{\partial}{\partial\tau}[\varepsilon_{yy} - \varepsilon_{zz}] + K(\xi-\tau)\frac{\partial}{\partial\tau}[2\varepsilon_{yy} + \varepsilon_{zz} - 3\varepsilon_T]\right\}d\tau \tag{46}$$

$$\sigma_{zz} = -P + \int_0^\xi \left\{-\frac{4}{3}G(\xi-\tau)\frac{\partial}{\partial\tau}[\varepsilon_{yy} - \varepsilon_{zz}] + K(\xi-\tau)\frac{\partial}{\partial\tau}[2\varepsilon_{yy} + \varepsilon_{zz} - 3\varepsilon_T]\right\}d\tau \tag{47}$$

From Eqs. (44) and (45), one can obtain that

$$\int_0^\xi K(\xi-\tau)\frac{\partial}{\partial\tau}[2\varepsilon_{yy}+\varepsilon_{zz}-3\varepsilon_T]d\tau = \int_0^\xi \frac{4}{3}G(\xi-\tau)\frac{\partial}{\partial\tau}[\varepsilon_{yy}-\varepsilon_{zz}]d\tau \tag{48}$$

Then substitution of Eq. (48) into Eq. (46) leads to

$$\sigma_{yy} = \int_0^\xi 2G(\xi-\tau)\frac{\partial}{\partial\tau}[\varepsilon_{yy} - \varepsilon_{zz}]d\tau \tag{49}$$

Once the strain components are obtained, Eq. (34) can be used to calculate the residual thermal birefringence as

$$\Delta n^{\text{th}} = n_y - n_z = \int_0^\xi C_\varepsilon(\xi-\tau)\frac{\partial}{\partial\tau}[\varepsilon_{yy} - \varepsilon_{zz}]d\tau \tag{50}$$

Solutions for the convolution integral and thermal birefringence are given in Appendix B.

In addition, it is important to mention that the through thickness strain of each melt layer satisfies a zero volumetric contraction due to the fact that the melt is added to the fluid core such that

$$\int_{-b}^{b} \varepsilon_{zz}(z)dz = 0 \tag{51}$$

The above equations are used to obtain the thermally-induced stresses and birefringence when the part is partially solidified with the core layers still being in the molten state and the outer layers in the solidified state. The melt pressure acts only when the molten resin is attached to the mold wall through the continuous molten core [21]. When the core vitrifies and all layers are in the solid state, the total through-thickness strain should also become constrained assuming a fixed value. Consequently, the pressure can no longer be prescribed but rather solved for till it vanishes. Otherwise, a higher prescribed pressure can cause over-constraint leading to an incorrect prediction of the thermal stresses [21]. To predict the thermal birefringence, the pressure and temperature fields are taken from the flow simulation.

2.4. Free quenching

The free quenching condition is employed when melt pressure drops to zero. Then the through thickness stress σ_{zz} equals to zero. The integration of the transverse stress σ_{yy} along the thickness direction leads to [15,22]

$$\sigma_{zz} = 0 \tag{52}$$

$$\int_{-b}^{b} \sigma_{yy}dz = 0 \tag{53}$$

where b is the half of thickness of cavity. The pressure term in Eq. (35) is removed and the linear viscoelastic constitutive equation becomes

$$\sigma_{ij} = \int_0^{\xi} \left\{ 2G(\xi-\tau)\frac{\partial}{\partial\tau}\left[\varepsilon_{ij} - \frac{1}{3}\varepsilon_{kk}\delta_{ij}\right] + \delta_{ij}K(\xi-\tau)\frac{\partial}{\partial\tau}[\varepsilon_{kk} - 3\varepsilon_T] \right\} d\tau \tag{54}$$

To solve the through thickness strain, the treatment similar to that used in deriving Eq. (B6) (see Appendix B) is employed. However, in this case the lateral strain, ε_{yy}, is no longer a fixed value. It can be solved by combining Eqs. (49) and (53). It should be noted that the Eq. (49) is still valid in case of free quenching. Therefore, by substituting Eq. (49) into Eq. (53), one obtains

$$\int_0^b \left\{ \int_0^{\xi} 2G(\xi-\tau)\frac{\partial}{\partial\tau}[\varepsilon_{yy} - \varepsilon_{zz}]d\tau \right\} dz = 0 \tag{55}$$

By using the piecewise continuous approximation, Eq. (55) becomes

$$\int_0^b \left\{ \sum_{i=1}^{k} 2G^{k,i}\left(\Delta\varepsilon_{yy}^i - \Delta\varepsilon_{zz}^i\right) \right\} dz = 0 \tag{56}$$

Separation of the kth term leads to

$$\varepsilon_{yy}^k = \frac{\int_0^b \left[G^{k,k}B^{k,k} - \mu^{k,i}\right] dz}{\int_0^b \left[G^{k,k}\left(1 - A^{k,k}\right)\right] dz} \tag{57}$$

Therefore, once the strain components ε_{zz}^k and ε_{yy}^k at the current time, k, are obtained from Eq. (B6) and Eq. (57), the lateral stress and birefringence can be calculated according to Eqs. (B9) and (B10). This algorithm is originally proposed for calculation of the residual thermal stress and birefringence in free quenching of amorphous [15] and semi-crystalline [22] polymers. However, use of free quenching assumption is too simplistic to describe the residual thermal stress and birefringence in the injection molding process, especially when the thermal stress and birefringence are comparable to that of the flow-induced stress and birefringence. In fact, for the molded parts of a complicated geometry or when a non-zero pressure exists in a cavity, the molded parts do not detach from the wall until the pressure drops to zero. Therefore, the constrained quenching is added to remedy this deficiency.

Once the flow and thermal birefringence is calculated, the total birefringence is assumed to be the summation of both as follows:

$$\Delta n = \Delta n^{\text{flow}} + \Delta n^{\text{th}} \tag{58}$$

The thermal strain ε_T, including volume relaxation, in a non-isothermal process can be described, as follows [23]:

$$\frac{d\varepsilon_T}{dt} = \alpha_g\frac{dT}{dt} - \frac{\varepsilon_T - \varepsilon_{Te}}{\tau_r a_T} \tag{59}$$

where ε_T and ε_{Te} are the actual and equilibrium thermal strain, respectively, at temperature T. The value of τ_r is the volume relaxation time at a reference temperature of T_r, with a_T being the modified shift factor for the volume relaxation and α_g is the linear expansion coefficient in the glassy state.

The modified form of the WLF equation is:

$$\log a_T = \frac{-C_1\left(T_{\text{eff}} - T_r\right)}{C_2 + T_{\text{eff}} - T_r} \tag{60}$$

where T_{eff} is the effective temperature, corresponding to the temperature when an equilibrium state has the same amount of free volume as the non-equilibrium state. This temperature is related to the actual temperature through

$$T_{\text{eff}} = T + \frac{\varepsilon_T - \varepsilon_{Tr}}{\alpha_1 - \alpha_g} \quad \text{if } T \geq T_2 \tag{61}$$

$$T_{\text{eff}} = T_2 + \frac{\varepsilon_T - \varepsilon_{Tr}}{\alpha_1 - \alpha_g} \quad \text{if } T < T_2 \tag{62}$$

The equilibrium thermal strain is given as:

$$\varepsilon_{Te} = \alpha_1(T - T_i) \quad \text{if } T \geq T_2 \tag{63}$$

$$\varepsilon_{Te} = \alpha_1(T_2 - T_i) + \alpha_g(T - T_2) \quad \text{if } T < T_2 \tag{64}$$

where α_l and α_g are the thermal expansion coefficients in the liquid and glassy states, respectively. The T_2 is the glass transition temperature observed at infinitely slow cooling rate. This temperature can be determined by the WLF equation as follows. The free volume, V_f, is defined as the difference of total macroscopic volume, V, and the actual volume, V_0.

$$V_f = V - V_0 \tag{65}$$

According to Doolittle [24] the relationship between the viscosity and the free volume is:

$$\log\eta = \log A + B\left(\frac{1}{f} - 1\right) \tag{66}$$

where A and B are constants and f is the fractional free volume defined as V_f/V. By using linear viscoelasticity, the shift factor is defined as:

$$\log a_T = \log\left[\frac{\eta(T)}{\eta(T_r)}\right] = \log\left[\frac{\tau(T)}{\tau(T_r)}\right] \tag{67}$$

where η and τ are viscosity and relaxation time, respectively. Then, Eq. (66) can be substituted into Eq. (67) to obtain

$$\log a_T = B\left[\frac{1}{f(T)} - \frac{1}{f(T_r)}\right] \tag{68}$$

From the PVT behavior of amorphous polymers, it is reasonable to assume that the equilibrium fractional free volume increases linearly with temperature at $T \geq T_2$. Then the fractional free volume becomes

$$f = \alpha_f(T - T_2) \tag{69}$$

where α_f is the thermal expansion coefficient of the fractional free volume above T_2. Substituting Eq. (69) into Eq. (68) results in

$$\log a_T = \frac{-B(T - T_r)}{\alpha_f(T_r - T_2)[(T_r - T_2) + T - T_r]} = \frac{-C_1(T - T_r)}{C_2 + T - T_r} \tag{70}$$

Accordingly, once the WLF equation is obtained, the T_2 can be taken as $C_2 - T_r$. Then, Eq. (50) and Eq. (54) can be used to evaluate the thermal birefringence. However, according to Eq. (60), the shift factor will become infinity when C_2 is equal to $T_r - T_{eff}$. For this reason, an additional assumption has to be made concerning the effective temperature $T < T_2$. Although in Eq. (60) the reference temperature can be chosen arbitrary, the effective temperature introduced is below T_g, since an additional non-equilibrium free volume appears in the temperature range

between T_g and T_{eff}. For that reason, the reference temperature T_r in Eq. (60) is chosen as T_g.

2.5. Anisotropic shrinkage in injection moldings

The volumetric shrinkage is predicted based on the specific volume, V, determined by the thermal and pressure history of the melt during the injection molding process. The volumetric shrinkage is calculated as [25]

$$S_V = \frac{\overline{V}_i - V_f}{\overline{V}_i} \tag{71}$$

where $\overline{V}_i$ is the initial specific volume of the melt and V_f is the final specific volume at room temperature. Since the polymer melt undergoes severe pressure and temperature changes in a short time, the initial specific volume cannot be assumed to be the same as that at constant pressure and temperature conditions. In the present simulation, the initial specific volume is calculated as

$$\overline{V}_i = \frac{1}{\left(t_p - t_f\right)} \int_{t_f}^{t_p} \overline{V}(t)\mathrm{d}t \tag{72}$$

where t_f is the time at the end of the filling stage, t_p is the packing time and $\overline{V}(t)$ is the time-dependent specific volume averaged through the gapwise direction for a particular cross section such that

$$\overline{V}(t) = \frac{1}{b} \int_0^b V(z,t)\mathrm{d}z \tag{73}$$

The specific volume is calculated from Tait equation of state, Eq. (37).

The shrinkage in the injection molded products is determined by cooling, pressure and elastic recovery effects [2,3]. The cooling causes all layers to experience the thermal contraction after ejection. In addition, each cross section solidifies under the packing pressure and therefore, at the end of the packing stage, tends to expand proportional to its value. At the end of packing stage, at the position where $T > T_g$, a recovery of the elastic strain that introduced during flow, occurs due to an abrupt pressure decay caused by the release of the packing pressure. Due to these three effects, the total shrinkage can be calculated as

$$S_i = \alpha_i\left(T_g - T_\infty\right) - \beta_i \overline{P} + S_{\gamma_\infty}, \quad i = x, y \tag{74}$$

where α_i is the linear thermal expansion coefficients. T_∞ is the ambient temperature, β_i is the compressibility, $\overline{P}$ is the average solidification pressure at each cross section, and S_{γ_∞} is the shrinkage that is due to the elastic recovery strain, γ_e, which is accumulated until the end of the packing stage. Values of α_i are evaluated based on biaxial orientation functions such that

$$\alpha_i = \alpha_0\left(1 - f_{or,i}\right) \tag{75}$$

in which $f_{or,i}$ is the orientation function in i direction, obtained as

$$f_{or,i} = \frac{\Delta n_i}{\Delta n^0} \tag{76}$$

where Δn_i is the calculated birefringence along i direction, and Δn^0 is the intrinsic birefringence.

$$S_{\gamma_\infty} = \int_0^{t_p} \dot{\gamma}_e(t)\mathrm{d}t \tag{77}$$

Simulations in [26] showed that the contribution of the compressibility to the anisotropic shrinkage in LGP moldings is negligible due to small difference introduced by the low value of the orientation function developed during molding. Also, at the processing conditions used in [26] the melt temperature at the end of packing stage has dropped below T_g at all points in the LGP cavity such that the contribution of the elastic recovery to shrinkage becomes negligible. Therefore, terms corresponding to compressibility and elastic recovery in Eq. (74) are dropped in calculation of shrinkage. Then, the shrinkage in the thickness direction is calculated based on the volumetric shrinkage and anisotropic in-plane shrinkage as

$$S_z \cong S_v - S_x - S_y \tag{78}$$

2.6. Numerical algorithm

The flow charts for calculation of the flow birefringence as well as the anisotropic shrinkage and the thermal birefringence are shown in Figs. 1 and 2, respectively. The numerical algorithm for simulation of flow in injection molding is based on CV/FEM/FDM scheme using a variable time step. The velocity, pressure, temperature and elastic strain tensor are calculated and updated at a new time step, $w + 1$. In the delivery system, contraction and expansion flows typically occurring due to the presence of junctions are neglected. Accordingly, the viscoelastic simulation in the delivery system is carried out based on one-dimensional viscoelastic flow. This simplification is done in order to avoid simulations of the two-dimensional contraction and expansion nonisothermal viscoelastic flow. It should be noted that to the best of our knowledge such

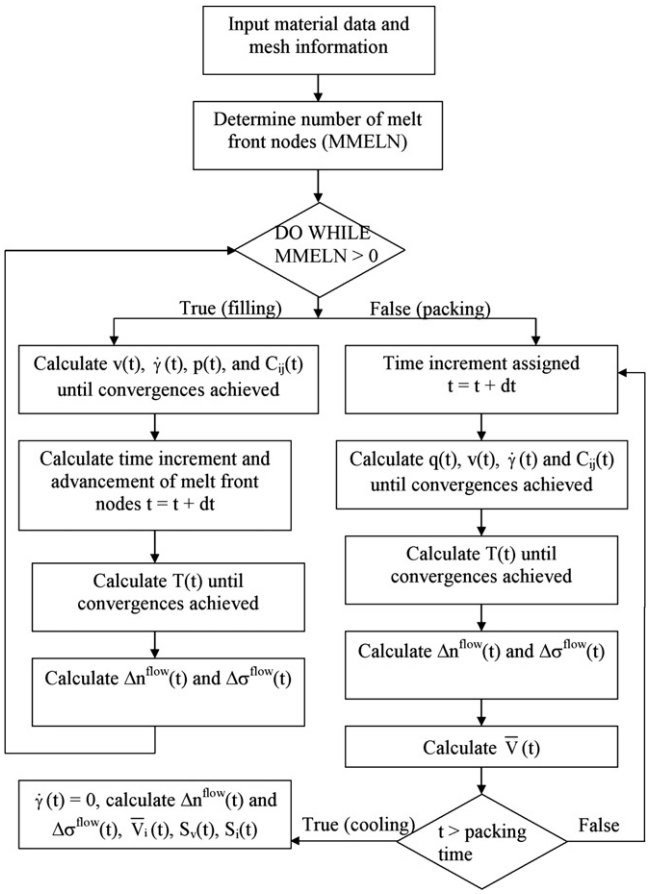

Fig. 1. Flow chart for calculation of the flow-induced birefringence and anisotropic shrinkage.

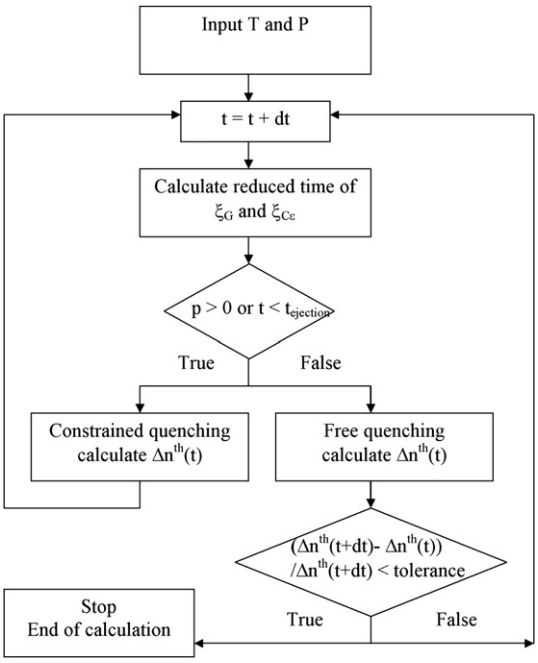

Fig. 2. Flow chart for calculation of the thermal birefringence.

viscoelastic simulations are not developed yet. The duration of each time step in the delivery system during the filling stage is obtained by calculating the time required for the current melt front to fill the next control volume. This volume is defined as the volume constructed by connecting the center point of two consecutive nodes, except for entrance and end nodes, as shown in Fig. 3. The large and small circles in Fig. 3 present, respectively, the nodes and center points of two consecutive nodes defining control volumes. In a two-dimensional flow, as occurs in disk or LGP cavity, the control volume of a node is determined by the volume defined by connecting the centroid of neighboring triangular elements, as indicated in Fig. 4. Therefore, the time step is determined as the shortest time required for the melt front to fill one of the neighboring control volumes. Fully filled, partially filled or empty nodes are shown in Fig. 4 by solid, shaded and empty circles, respectively. The arrows indicate the direction of melt front propagation.

Once the time step is calculated, the melt front nodes to be fully filled, partially filled or empty are determined and then, the pressure is iteratively solved according to Eqs. (A3) and (A7). To apply these equations for calculation of the pressure field, the Tait equation of state, Eq. (37), along with calculated time step are used to evaluate the G and H by using Eqs. (28) and (29). However, the fluidities, S_i in Eqs. (30) and (31) are coupled with shear rates and shear rates in Eqs. (23) and (24) are related to velocities in Eqs. (25) and (26) and the elastic strain tensor components in Eqs. (9a)–(9f). Therefore, an iterative process is required to solve these equations simultaneously to determine S_i. To initiate this process, initial guesses for the elastic strain tensor components are required. Accordingly, the steady state solution

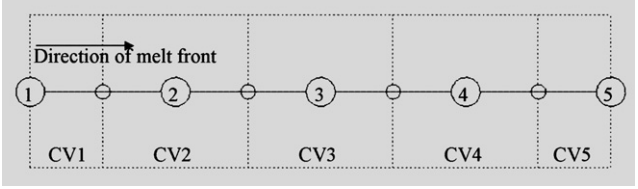

Fig. 3. Time step in an one-dimensional flow is determined as the time required to fully fill a control volume. (Large circles: nodes, small circles: boundary of control volumes, dashed line: control volume).

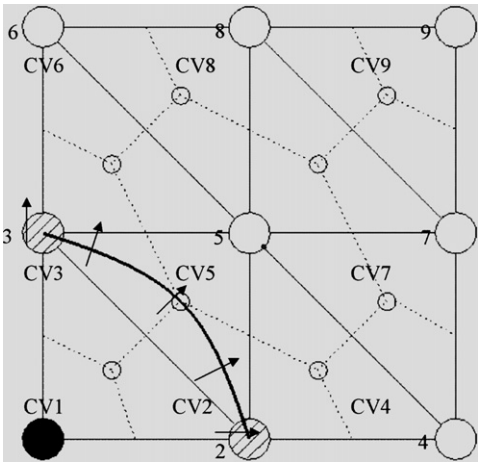

Fig. 4. Time step in a two-dimensional flow is determined as the shortest time required to fully fill one of the neighboring control volumes. (Solid circles: fully-filled node, shaded circles: partially-filled node, open circles: empty node).

of the elastic strain tensor components is used for the initial guesses at each calculated node except for the entrance node. For the entrance node, since the temperature is fixed until the end of packing stage, it is reasonable to take the steady state solution of the elastic strain tensor components of Eqs. (9a)–(9f). Therefore, Eqs. (23)–(26) and Eqs. (9a)–(9f) can be solved simultaneously until shear rates are converged. The calculated shear rates are then used to evaluate S_i in Eqs. (30) and (31). Then, the pressure is obtained by Eqs. (A3) and (A7). Once the new pressure of node m, $p_m^{w+1,\mathrm{new}}$, is obtained, the under relaxation method [16] is used to calculate the updated pressure according to

$$p_m^{w+1,\mathrm{update}} = (1-\omega_p)p_m^{w+1,\mathrm{old}} + \omega_p p_m^{w+1,\mathrm{new}} \tag{79}$$

where ω_p is the weighting factor varying from 0 to 1. Typically, this value in the present study is between 0.7 and 0.8. If the $p_m^{w+1,\mathrm{new}}$ is not equal to $p_m^{w+1,\mathrm{update}}$, the entire process repeated until a convergence is reached.

In addition, the calculation of temperature field should be also incorporated into the iteration process for pressure calculation since the relaxation time, η_k, and viscosity, θ_k, are temperature dependent, as indicated in Eqs. (18) and (19). To simplify the calculation, the temperature obtained in the wth time step is used for the entire pressure iteration. After the velocity, pressure and elastic strain tensor fields are obtained, the energy equation, Eq. (4), is solved for the temperature field at time step $w+1$ by using under relaxation method as

$$T_m^{w+1,\mathrm{update}} = (1-\omega_T)T_m^{w+1,\mathrm{old}} + \omega_p T_m^{w+1,\mathrm{new}} \tag{80}$$

where ω_T is the weighting factor varying from 0 to 1. This algorithm is continued until the end of the filling stage.

In the packing stage, the algorithm is similar to the filling stage, but the time steps are assigned rather than solved for, since no melt front propagation is involved in this stage. It should be noted that Eqs. (A3) and (A7) are still valid. The pressure at the entrance is equal to the applied packing pressure. The flow rate at the entrance, Q_{c1}, is calculated. The obtained velocity, pressure and elastic strain tensor fields are used to calculate the flow rate by summation of

Table 1
Processing condition for the injection molding of PS disc.

Flow rate (cm^3/s)	Melt temperature (°C)	Mold temperature (°C)	Packing pressure (MPa)	Packing time (s)
23.8	225	40	15	6

Table 2
Material specification and parameters for PS Styron 615.

WLF equation		Refs.
C_1	8.285	
C_2(K)	131.90	[30]
T_r(K)	473.5	
Rheological model		[30]
s	0.00484	
T_r(K)	473.5	
η_1(Pa s)	2228	
θ_1(s)	0.1466	
η_2(Pa s)	446.8	
θ_2(s)	0.00489	
Tait equation		[37]
b_{1l} (m^3/Kg)	9.799e−4	
b_{1s}(m^3/Kg)	9.799e−4	
b_{2l} (m^3/Kg K)	5.788e−7	
b_{2s} (m^3/Kg K)	2.429e−7	
b_{3l} (N/m^2)	4.615e−8	
b_{3s} (N/m^2)	3.301e−8	
b_{4l} (K^{-1})	3.019e−3	
b_{4s} (K^{-1})	1.380e−3	
b_5(K)	376.0	
b_6(K/Pa)	3.20e−7	
Δn^0	−0.195	[38]
C_σ (Pa^{-1})	−5.2E−9	[14]
k (J/m s K)	0.122	[37]
C_p (J/Kg K)	2050	[37]

flow rates in each node at the melt front, Q_{c2}. The convergence reaches when Q_{c1} is equal to Q_{c2}.

In the cooling stage, the shear rate and velocity are zero. Therefore, the energy equation, Eq. (4), reduces to a one-dimensional transient heat conduction equation:

$$\rho C_p \frac{\partial T}{\partial t} = \frac{\partial}{\partial z}\left(k \frac{\partial T}{\partial z}\right) \tag{81}$$

The governing equation for the elastic strain tensor, Eq. (8), reduces to

$$\frac{\partial \mathbf{C}_k}{\partial t} + \frac{1}{2\theta_k}\left[\mathbf{C}_k^2 + \frac{1}{3}\left(II_C^k - I_C^k\right)\mathbf{C}_k - I\right] = 0 \tag{82}$$

In the cooling stage, the relaxation process occurs, since no more pressure is applied. The initial conditions for $\boldsymbol{C}_k$ and T correspond to

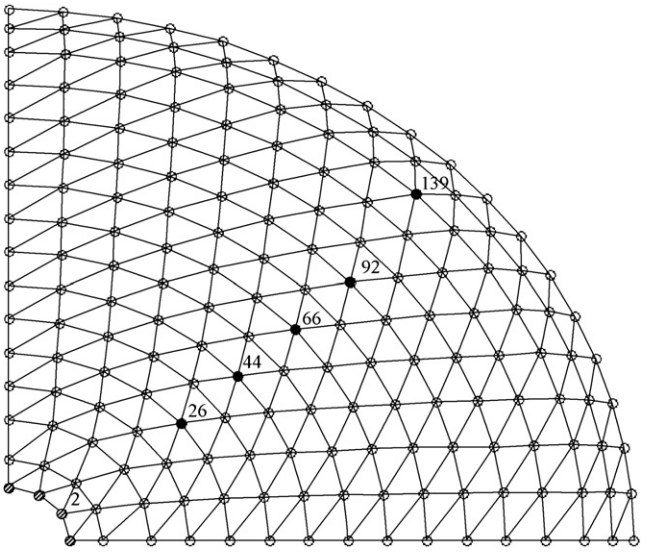

Fig. 5. Finite element mesh used in simulation of a disk injection molding. The crosshatched, open and filled circles represent, respectively, the entrance nodes, nodes and nodes where the simulated results are compared.

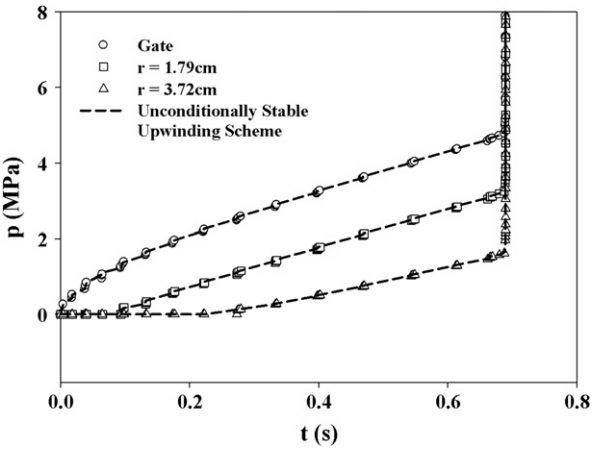

Fig. 6. Comparison of calculated pressure traces during the filling stage and at the onset of the packing stage at various locations by the conventional scheme (symbols), used in [30], and the unconditionally stable upwinding scheme (curves) of the present study.

their values of at the end of the packing stage. The Eq. (81) is solved by implicit method to obtain the temperature field. The Euler method [27] is used to integrate Eq. (82) to obtain the elastic strain tensor components.

In order to avoid a cumbersome numerical calculation in a two-dimensional flow, the governing equations for the elastic strain tensor,$\boldsymbol{C}_k$, Eqs. (9a)–(9f), are rewritten in the streamwise coordinate system and discretized as given in Appendix C. Then, the set of discretized equations are solved by means of Newton–Raphson method at each time step. The resulting C_{ij} tensor components are used to calculate new shear rates until a convergence is met. The initial guess of C_{ij} tensor is taken as an average value from upwind nodes [28,29]. To determine the upwinding nodes correctly, the sequence of calculation is essential to ensure that the calculated sequence of C_{ij} is always from downstream nodes. In case of a one-dimensional flow, the solution is straightforward since the sequence of calculation is the same as the sequence of nodes numbering. However, in case of a two-dimensional flow it becomes complicated, since the numbering of node is arbitrary. To resolve this issue, the calculated nodal pressures are used to indicate the sequence of calculations, since the flow always takes place from

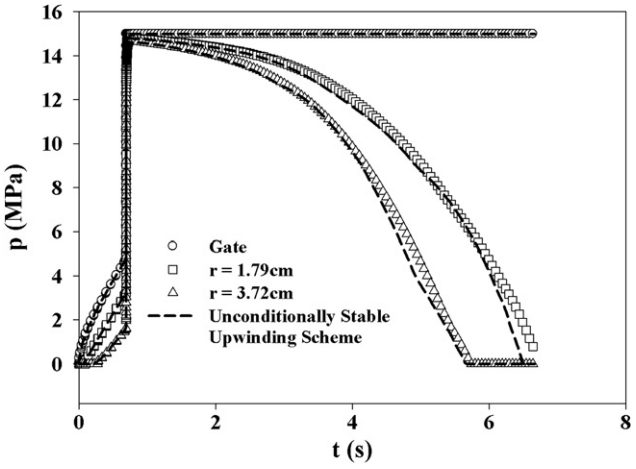

Fig. 7. Comparison of calculated pressure traces during the filling and packing stages at various locations by the conventional scheme (symbols), used in [30], and the unconditionally stable upwinding scheme (curves) of the present study.

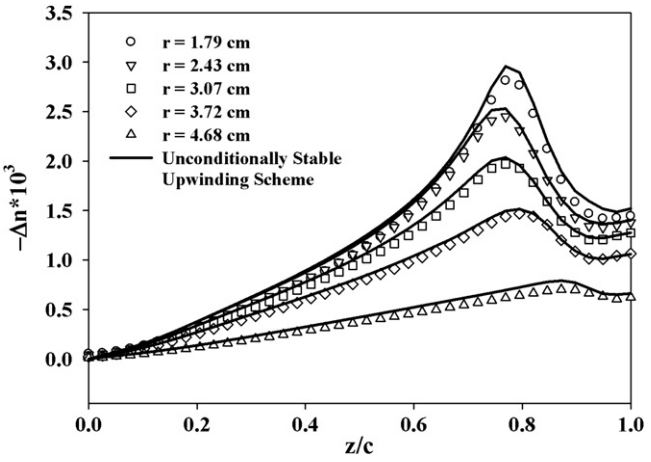

Fig. 8. Calculated gapwise birefringence at the end of filling stage at various locations by the conventional scheme (symbols), used in [30], and the unconditionally stable upwinding scheme (curves) of the present study.

a high to low pressure location. Therefore, the calculated pressure from the previous time step is compared with that at the beginning of current time step. This way the sequence of calculations is determined.

2.7. Numerical test

To verify the new numerical scheme, a numerical test for an injection molding of a PS disc is carried out to compare the present simulated results with those given in [30]. Table 1 shows the processing condition used in this test. The material parameters used in this test are given in Table 2. It is seen from Table 2 that rheological model for PS melt is represented by two relaxation modes. Generally, two relaxation modes are insufficient for the description of flow in injection molding occurring in wide range of shear rates. However, in the present paper this is done in order to provide the exact comparison with earlier simulated results [30] obtained using the same two relaxation modes. Larger number of relaxation modes will be introduced in Part 2 of this study where extensive comparisons of simulated results with experimental data will be carried out for LGP moldings.

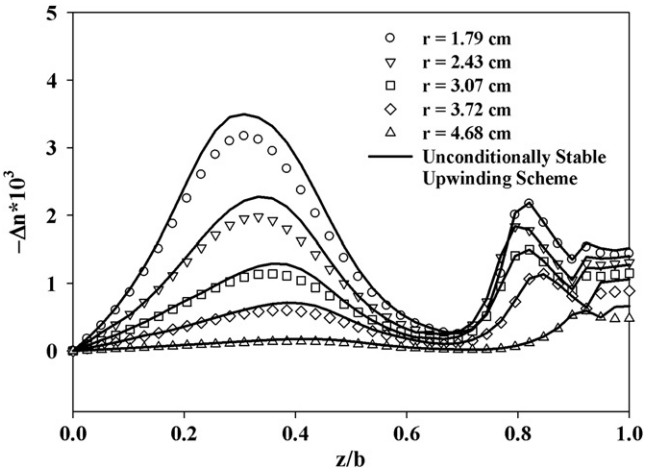

Fig. 9. Calculated gapwise birefringence at the end of packing stage at various locations by the conventional scheme (symbols), used in [30], and the unconditionally stable upwinding scheme (curves) of the present study.

Fig. 5 shows the finite element mesh of a quarter disc molding in which 315 linear triangular elements and 184 nodes are used in the planar direction with 40 evenly spaced finite difference grids in the gapwise direction. The radius and thickness of the disk are 5.08 cm and 0.2 cm, respectively. Also, in the Fig. 5, the global nodal numbers of 26, 44, 66, 92 and 139 correspond to the radius of 1.79, 2.43, 3.07, 3.72 and 4.68 cm, respectively. Simulated data at these positions reported in [30] are used for comparison with the present simulated results.

Fig. 6 shows a comparison of pressure traces during the filling stage and at the onset of packing stage at the gate and at radii of 1.79 and 3.72 cm calculated by conventional numerical scheme (symbols), used in [30], and unconditionally stable upwinding scheme (curves), used in the present study. Fig. 7 indicates the calculated pressure traces during the filling and the entire packing stage at the same locations. Nearly identical values are observed in the filling stage, but a slight deviation occurs at locations of 1.79 and 3.72 cm at the end of the packing stage. In particular, the results calculated by unconditionally stable upwinding scheme exhibit a slightly faster pressure relaxation than the conventional scheme.

Fig. 8 demonstrates the calculated gapwise birefringence at the end of filling stage at various locations by the conventional scheme (symbols), used in [30], and the unconditionally stable upwinding scheme (curves), used in the present study. The Δn calculated by the unconditionally stable upwinding scheme shows only slightly higher values of birefringence than that calculated by the conventional scheme.

Fig. 9 shows the calculated gapwise birefringence at the end of the packing stage at various locations by conventional scheme (symbols), used in [30], and the unconditionally stable upwinding scheme (curves), used in the present study. Again, the Δn calculated by the unconditionally stable upwinding scheme shows slightly higher values of birefringence. The largest deviation of 9.2% occurs at the maximum birefringence occurring at a radius of 1.79 cm.

Although a slight deviation between numerical results obtained by two algorithms is observed, the calculation time is reduced from 2 h to 30 min by using the unconditionally stable upwinding scheme. This is due to the fact that a subdivision of the time step is required for the conventional upwinding scheme, if Eq. (C9) is not satisfied. That means the current time step has to be divided by 2 and the entire calculation has to be repeated. If the convergence is still not met, the same procedure has to be carried out again. In fact, when the number of elements and the local velocity are large, the time saving is substantial due to complete elimination of the subdivision of time step.

3. Conclusion

Based on the numerical test presented in this study, it can be concluded that the unconditionally stable upwinding scheme for viscoelastic simulation of injection molding process is more efficient and resulted in similar predicted pressure traces and flow birefringence as the conventional upwinding scheme. It is shown that the proposed numerical scheme is able to provide a significantly faster solution. Therefore, it is more feasible for use in future commercial applications. Also, it should noted, as will be shown in the subsequent paper, the simulation of the total frozen-in birefringence in moldings determined by summation of the frozen-in flow birefringence, calculated by using a nonlinear viscoelastic constitutive equation, and the thermal birefringence based on combination of both constrained and free quenching and calculated by using linear viscoelastic and photoviscoelastic constitutive equations provides a better agreement with experimental data.

Acknowledgement

The authors greatly appreciate the financial support of the NSF Division of Engineering under grant DMI-0322920.

Appendix A. Numerical solution of Hele-Shaw equations

To obtain the FEM forms, the linear shape functions are applied to Eqs. (27) and (32) [31,32]. In case of two-dimensional triangular elements, the pressure field can be expressed through the linear shape functions leading to the following FEM form of Eq. (27):

$$G^l A^l \sum_{n=1}^{3} E_{iN} \frac{P_i^w - P_i^{w+1}}{\Delta t} + S^l \sum_{n=1}^{3} D_{iN}^l P_i^{w+1} = -\frac{A^l H^l}{3} \tag{A1}$$

where subscript i presents local node number, $i = 1, 2, 3$, and the subscipt l represents global element number. The A^l denotes the element area and w and $w+1$ is a current and new time step, respectively, and

$$E_{iN} = \begin{cases} 1/6 & \text{if } i = N \\ 1/12 & i \neq N \end{cases} \quad D_{iN}^l = \frac{1}{4A^l}\left[b_{2i}^l b_{2N}^l + b_{3i}^l b_{3N}^l\right] \tag{A2}$$

where b_{ij}^l indicates weighting factors for $i = 1, 2, 3$. Eq. (A1) is the FEM form of the governing equation suitable for introducing the concept of control volume. If one assumes G^l is evaluated at each node M, as G_M, separation of the diagonal and off-diagonal components, leads to

$$\begin{aligned} \sum_{l=1}^{CV}\left(\frac{A^l G_M}{\Delta t} E_{qq} + S^l D_{qq}^l\right) P_M^{w+1} = & \sum_{l=1}^{CV}\left(\frac{A^l G_M}{\Delta t} \sum_{\substack{k=1 \\ (k\neq q)}}^{3} E_{qk}^l \left(P_N^w - P_N^{w+1}\right)\right) \\ & - \sum_{l=1}^{CV} S^l \sum_{\substack{k=1 \\ (k\neq q)}}^{3} \left(D_{qk}^l P_N^{w+1}\right) \\ & + \sum_{l=1}^{CV} \frac{A^l G_M}{\Delta t} E_{qq}^l P_M^w - \sum_{l=1}^{CV} \frac{A^l H^l}{3} + \frac{Q_M}{2} \end{aligned} \tag{A3}$$

where $M = \text{NELNOD}(l, q)$ and $N = \text{NELNOD}(l, k)$. The function $M = \text{NELNOD}(l, q)$ indicates the global node number M of the local qth node of element l. In Eq. (A3)

$$\begin{array}{lll} Q_M = 0 & & \text{Fully-filled nodes} \\ Q_M = Q_{\text{Ent}} & \text{for} & \text{Entrance nodes} \\ Q_M = Q_{MF} & & \text{Melt front nodes} \end{array} \tag{A4}$$

Now, the governing Eq. (A3) can be used to solve for pressure field in a two-dimensional flow by under relaxation iteration [16].

To obtain the FEM form of governing equation in a one-dimensional flow (Eq. (32)), the pressure field can be expressed through the linear shape functions leading to the following FEM form

$$\frac{G^l L^l}{2} \sum_{n=1}^{2} E_{iN} \frac{P_i^w - P_i^{w+1}}{\Delta t} + S^l \sum_{n=1}^{2} D_{iN}^l P_i^{w+1} = -\frac{L^l H^l}{2} \tag{A5}$$

where L^l is the length of the one-dimensional element, and

$$E_{iN} = \begin{cases} 2/3 & \text{if } i = N \\ 1/3 & i \neq N \end{cases} \quad D_{iN}^l = \frac{1}{L^l}\begin{bmatrix} 1 & -1 \\ -1 & 1 \end{bmatrix} \tag{A6}$$

Similar to Eq. (A1), Eq. (A5) can be discretized by separation of the diagonal and off-diagonal components to obtain

$$\begin{aligned} \sum_{l=1}^{CV}\left(\frac{L^l G_M}{2\Delta t} E_{qq} + S^l D_{qq}^l\right) P_M^{w+1} = & \sum_{l=1}^{CV}\left(\frac{L^l G_M}{2\Delta t} \sum_{\substack{k=1 \\ (k\neq q)}}^{2} E_{qk}^l \left(P_N^w - P_N^{w+1}\right)\right) \\ & - \sum_{l=1}^{CV} S^l \sum_{\substack{k=1 \\ (k\neq q)}}^{2} \left(D_{qk}^l P_N^{w+1}\right) \\ & + \sum_{l=1}^{CV} \frac{L^l G_M}{2\Delta t} E_{qq}^l P_M^w - \sum_{l=1}^{CV} \frac{L^l H^l}{2} + \frac{Q_M}{2} \end{aligned} \tag{A7}$$

The conditions on Q_M are the same as in Eq. (A4). Accordingly, the control-volume finite element method [31–33] with triangular and linear elements with linear shape functions is used to solve for the pressure field by using Eqs. (A3) and (A7), respectively. It should be noted that G and H are constant in each control volume; S_x and S_y are constant in each element. In addition, it has to be noted that Eqs. (A3) and (A7) are used in both the filling and packing stages. The only difference is that in the filling stage the flow rate is assigned at entrance nodes to solve for pressure, while in the packing stage the flow rate is calculated at specified entrance pressure.

Appendix B. Solution for convolution integral

Constrained quenching

To solve the convolution integral of Eq. (48), the piecewise continuous approximation [34] was used to obtain the through thickness strain. This approximation can be used only when the change of strain is small enough such that

$$\int_0^t f(\xi - \tau)\frac{\partial q(\tau)}{\partial \tau} d\tau = \sum_{i=1}^{k}\left(\Delta q^i f^{k,i}\right) \tag{B1}$$

in which

$$\Delta q^i = q(t^i) - q(t^{i-1}) \quad \text{and} \quad f^{k,i} = \frac{1}{\Delta t^i}\int_{t^{i-1}}^{t^i} f(\xi - \tau) d\tau \tag{B2}$$

Therefore, the integrals in Eq. (48) can be discretized as

$$\int_0^{\xi} G(\xi - \tau)\frac{\partial \varepsilon_{yy}}{\partial \tau} d\tau = \sum_{i=1}^{k}\left(\Delta \varepsilon_{yy}^i G^{k,i}\right) \tag{B3}$$

in which

$$\Delta \varepsilon_{yy}^i = \varepsilon_{yy}\left(\xi^i\right) - \varepsilon_{yy}\left(\xi^{i-1}\right) \text{ and } G^{k,i} = \frac{1}{\Delta \xi^i}\int_{\xi^{i-1}}^{\xi^i} G(\xi - \tau) d\tau \tag{B4}$$

Accordingly, Eq. (48) becomes

$$\frac{4}{3}\sum_{i=1}^{k}\left[G^{k,i}\left(\Delta \varepsilon_{zz}^i - \Delta \varepsilon_{yy}^i\right)\right] + \sum_{i=1}^{k}\left[K^{k,i}\left(2\Delta \varepsilon_{yy}^i + \Delta \varepsilon_{zz}^i - 3\Delta \varepsilon_T^i\right)\right] = 0 \tag{B5}$$

Separation of the kth term corresponding to the current time step generates

$$\varepsilon_{zz}^{k} = -\left(\frac{4G^{k,k}-6K^{k,k}}{4G^{k,k}+3K^{k,k}}\right)\varepsilon_{yy}^{k} + \left(\frac{4\mu^{k,i}-3\lambda^{k,i}}{4G^{k,k}+3K^{k,k}}\right) = A^{k,k}\varepsilon_{yy}^{k} + B^{k,k} \quad \text{(B6)}$$

in which

$$\mu^{k,i} = -G^{k,k}\left(\varepsilon_{yy}^{k-1} - \varepsilon_{zz}^{k-1}\right) + \sum_{i=1}^{k-1}\left[G^{k,i}\left(\Delta\varepsilon_{zz}^{i} - \Delta\varepsilon_{yy}^{i}\right)\right] \quad \text{(B7)}$$

$$\lambda^{k,i} = -K^{k,k}\left(I_{\varepsilon}^{k-1} + 3\Delta\varepsilon_{T}^{k}\right) + \sum_{i=1}^{k-1}\left[K^{k,i}\left(\Delta I_{\varepsilon}^{i} - 3\Delta\varepsilon_{T}^{i}\right)\right] \quad \text{(B8)}$$

Therefore, the strain components are fully determined. By applying the same treatment to Eq. (49), one obtains

$$\sigma_{y} = \sum_{i=1}^{k} 2G^{k,i}\left(\Delta\varepsilon_{yy}^{i} - \Delta\varepsilon_{zz}^{i}\right) = 2\left[\mu^{k,i} + G^{k,k}\left(\varepsilon_{yy}^{k} - \varepsilon_{zz}^{k}\right)\right] \quad \text{(B9)}$$

Applying the piecewise continuous approximation to Eq. (50) leads to

$$\Delta n^{th} = \sum_{i=1}^{k} C_{\varepsilon}^{k,i}\left(\Delta\varepsilon_{yy}^{i} - \Delta\varepsilon_{zz}^{i}\right) = \sum_{i=1}^{k}\frac{\Delta\varepsilon_{yy}^{i} - \Delta\varepsilon_{zz}^{i}}{\xi^{i} - \xi^{i-1}}\int_{\xi^{i-1}}^{\xi^{i}} C_{\varepsilon}(\xi-\tau)\mathrm{d}\tau \quad \text{(B10)}$$

Eq. (B10) is used to calculate the thermally-induced birefringence after obtaining strain components.

Appendix C. Governing equations for C_k in the streamwise coordinates

By introducing the streamwise coordinate system (s, θ, z) [16], where s is the streamwise direction, θ is perpendicular to the s in the counterclockwise direction, and z is the gapwise direction, Eqs. (9a)–(9f) reduce to

$$\frac{DC_{ss,k}}{Dt} - 2C_{sz,k}\frac{\partial v_s}{\partial z} + \frac{1}{2\theta_k}\left(C_{ss,k}^{2} + C_{sz,k}^{2} - 1\right) = 0 \quad \text{(C1)}$$

$$\frac{DC_{sz,k}}{Dt} - C_{zz,k}\frac{\partial v_s}{\partial z} + \frac{1}{2\theta_k}\left(C_{ss,k}C_{sz,k} + C_{zz,k}C_{sz,k}\right) = 0 \quad \text{(C2)}$$

$$\frac{DC_{zz,k}}{Dt} + \frac{1}{2\theta_k}\left(C_{sz,k}^{2} + C_{zz,k}^{2} - 1\right) = 0 \quad \text{(C3)}$$

$$\det|\mathbf{C}_k| = C_{ss,k}C_{zz,k} - C_{sz,k}^{2} = 1 \quad \text{(C4)}$$

in which only three elastic strain tensor components left to be solved instead of five. Components of the elastic strain tensor in a global coordinate system are recovered as

$$C_{xx,k} = C_{ss,k}\cos^{2}\phi + \sin^{2}\phi \quad \text{(C5)}$$

$$C_{yy,k} = C_{ss,k}\sin^{2}\phi + \cos^{2}\phi \quad \text{(C6)}$$

$$C_{xz,k} = C_{sz,k}\cos\phi \quad \text{(C7)}$$

$$C_{yz,k} = -C_{sz,k}\sin\phi \quad \text{(C8)}$$

where ϕ is the angle between vector x and s.

Eqs. (C1)–(C4) indicate a set of elliptic partial differential equations (PDEs). To solve these PDEs, the upwinding finite difference scheme is applied [32] in which the forward difference is used to discretize time variable, and the backward difference for space variable. However, such an algorithm can be only stable at the following condition:

$$\frac{v_s\mathrm{d}t}{\mathrm{d}s} < 1 \quad \text{(C9)}$$

Therefore, a very small time step is required, especially at high velocities. If the current time step is large, then a subdivision of the time step is required. This introduces significant calculation effort and limits the ability of handling various processing conditions. Accordingly, an unconditionally stable upwinding scheme [13] is used to remedy this limitation and reduce the calculation time. With this new proposed unconditionally stable upwinding scheme, the forward difference is still used to discretize time variable, but the backward difference is used to discretize space variable at $t+1$. If $t+1$ presents the current time and t is the previous time, Eqs. (C1)–(C4) result in a nonlinear system of equations:

$$F_1 = C_{ss,i}^{t+1} - C_{ss,i}^{t} + \frac{\Delta t}{\Delta s}v_s\left(C_{ss,i}^{t+1} - C_{ss,i-1}^{t+1}\right) - 2\Delta t\dot{\gamma}C_{sz,i}^{t+1} + \frac{\Delta t}{2\theta_k}\left(C_{ss,i}^{t+1}\cdot C_{ss,i}^{t+1} + C_{sz,i}^{t+1}\cdot C_{sz,i}^{t+1} - 1\right) = 0 \quad \text{(C10)}$$

$$F_2 = C_{sz,i}^{t+1} - C_{sz,i}^{t} + \frac{\Delta t}{\Delta s}v_s\left(C_{sz,i}^{t+1} - C_{sz,i-1}^{t+1}\right) - \Delta t\dot{\gamma}C_{zz,i}^{t+1} + \frac{\Delta t}{2\theta_k}\left(C_{ss,i}^{t+1}\cdot C_{sz,i}^{t+1} + C_{sz,i}^{t+!}\cdot C_{zz,i}^{t+1}\right) = 0 \quad \text{(C11)}$$

$$F_3 = C_{zz,i}^{t+1} - C_{zz,i}^{t} + \frac{\Delta t}{\Delta s}v_s\left(C_{zz,i}^{t+1} - C_{zz,i-1}^{t+1}\right) + \frac{\Delta t}{2\theta_k}\left[\left(C_{sz,i}^{t+1}\right)^{2} + \left(C_{zz,i}^{t+1}\right)^{2} - 1\right] = 0 \quad \text{(C12)}$$

To solve this nonlinear system of equations, the Newton–Raphson method [35,36] is used as follows

$$-F(X_n) = J(X_n)(X_{n+1} - X_n) \quad \text{(C13)}$$

where

$$F = [F_1 \quad F_2 \quad F_3]^{T} \quad \text{(C14)}$$

$$X_n = \left[C_{ss}^{t+1} \quad C_{sz}^{t+1} \quad C_{zz}^{t+1}\right]^{T} \quad \text{(C15)}$$

and J is the Jacobian matrix defined as

$$J = \begin{bmatrix} \frac{\partial F_1}{\partial C_{ss}^{t+1}} & \frac{\partial F_1}{\partial C_{sz}^{t+1}} & \frac{\partial F_1}{\partial C_{zz}^{t+1}} \\ \frac{\partial F_2}{\partial C_{ss}^{t+1}} & \frac{\partial F_2}{\partial C_{sz}^{t+1}} & \frac{\partial F_2}{\partial C_{zz}^{t+1}} \\ \frac{\partial F_3}{\partial C_{ss}^{t+1}} & \frac{\partial F_3}{\partial C_{sz}^{t+1}} & \frac{\partial F_3}{\partial C_{zz}^{t+1}} \end{bmatrix} \quad \text{(C16)}$$

References

[1] Isayev AI, Shyu GD, Li CT. Residual stresses and birefringence in injection molding of amorphous polymers. J Polym Sci Polym Phys 2006;44:622–39.
[2] Kwon K, Isayev AI, Kim KH. Toward a viscoelastic modelling of anisotropic shrinkage in injection molding of amorphous polymers. J Appl Polym Sci 2005;98:2300–13.
[3] Isayev AI, Kwon K. Volumetric and anisotropic shrinkage in injection moldings of thermoplastics. In: Kamal MR, Isayev AI, Liu S-J, editors. Book injection molding: technology and fundamentals. Munich: Hanser; 2009. p. 779–808 [Chapter 19].

[4] Lin CS, Wu WZ, Lay YL, Chang MW. A digital image-based measurement system for a LCD backlight module. Opt Laser Technol 2001;33:499–505.
[5] Okumura T, Tagaya A, Koike Y. Highly-efficient backlight for liquid crystal display having no optical films. Appl Phys Lett 2003;83(13):2515–7.
[6] Leutz R, Ries H. Microstructured light-guides overcoming the two-dimensional concentration limit. Appl Opt 2005;44(32):6885–9.
[7] Lin TH, Isayev AI, Mehranpour M. Luminance of injection molded V-groove light guide plates. Polym Eng Sci 2008;48:1615–23.
[8] Han X, Yokoi H, Takahashi T. Effects of cavity conditions on transcription molding of microscale prism patterns using ultra-high speed injection molding. Int Polym Process XXI 2006;5:473–9.
[9] Feng D, Jin G, Yan Y, Fan S. High quality light guide plates that can control the illuminance angle based on microprism structures. Appl Phys Lett 2004;85:6016–8.
[10] Feng D, Yan Y, Yang X, Jin G, Fan S. Novel integrated light-guide plates for liquid crystal display backlight. J Opt A Pure Appl Opt 2005;7:111–7.
[11] Leonov AI. Nonequilibrium thermodynamics and rheology of viscoelastic polymer media. Rheol Acta 1976;15:85–98.
[12] Janeschitz-Kriegl H. Polymer melt rheology and flow birefringence. New York: Springer; 1983.
[13] Ames WF. Numerical methods for partial differential equations. 3rd ed. Boston: Academic Press; 1992.
[14] Shyu GD, Isayev AI, Li CT. Photoviscoelastic behavior of amorphous polymers during transition from the glassy to rubbery state. J Polym Sci Phys Ed 2001;39:2252–62.
[15] Shyu GD, Isayev AI, Li CT. Residual thermal birefringence in freely quenched plates of amorphous polymers: simulation and experiment. J Polym Sci Phys Ed 2003;41:1850–67.
[16] Sobhanie M, Isayev AI. Viscoelastic simulation of flow of rubber compounds. Rubber Chem Technol 1989;62:939–56.
[17] Dill EH. On phenomenological rheo-optic constitutive relations. J Polym Sci Part C Polym Symposia 1964;5:67.
[18] Morland LW, Lee EH. Stress analysis for linear viscoelastic materials with temperature variation. Trans Soc Rheol 1960;4:233–63.
[19] Van Krevelen DW, Hoftyzer PJ. Properties of polymers. Amsterdam: Elsevier; 1976. pp. 271.
[20] Lee YB, Kwon TH, Yoon K. Numerical prediction of residual stresses and birefringence in injection/compression molded center-gated disk. Part I: basic modeling and results for injection molding. Polym Eng Sci 2002;42:2246–72.
[21] Ghoneim H, Hieber CA. Incorporation of density relaxation in the analysis of residual stresses in molded parts. Polym Eng Sci 1997;37:219–27.
[22] Guo X, Isayev AI. Residual stresses and birefringence in injection molding of semicrystalline polymer, part 1: theoretical formulation. Intern Polym Process 1999;14:377–86.
[23] Rusch KC. Time–temperature superposition and relaxation behavior in polymeric glasses. J Macromolecular Sci Phys 1968;B2:179.
[24] Doolittle AK. Studies in newtonian flow. II. The dependence of the viscosity of liquids on free-space. J Appl Phys 1953;22:12.
[25] Isayev AI, Hariharan T. Volumetric effects in the injection molding of polymers. Polym Eng Sci 1985;25:271–8.
[26] Isayev AI, Lin TH. Birefringence, anisotropic shrinkage and luminance in light guide plates: modeling and experiment. SPE Tech Pap 2007;53:2485–9.
[27] Carnahan B, Luther HA, Wilkes JO. Applied numerical methods. New York: Wiley; 1969.
[28] Paillere H, Boxho J, Degrez G, Deconinck H. Multidimensional upwind residual distribution schemes for the convection-diffusion equation. Int J Numer Methods Fluids 1996;23:923–36.
[29] Carette JC, Deconinck H, Paillere H, Roe PL. Multidimensional upwinding: its relation to finite elements. Numer Methods Fluid 1995;20:935–55.
[30] Shyu GD, Isayev AI, Lee HS. Numerical simulation of flow-induced birefringence in injection molded disk. Korea-Australia Rheol J 2003;15:159–66.
[31] Wang VW, Hieber CA, Wang KK. Dynamic simulation and graphics for the injection molding of three-dimensional thin parts. J Polym Eng 1986;7:21–45.
[32] Isayev AI. Modeling of polymer processing: recent development. Munich: Hanser; 1991.
[33] Chiang HH, Hieber CA, K Wang K. A unified simulation of the filling and postfilling stages in injection molding. Part I: formulation. Polym Eng Sci 1991;31:125–39.
[34] Narayanaswamy OS, Gardon R. Calculation of residual stresses in glass. J Am Ceram Soc 1969;52:554–8.
[35] Anderson JD. Computational fluid mechanics. McGraw-Hill; 1995.
[36] Press WH, Teukolsky SA, Vetterling WT, Flannery BP. Numerical recipes in fortran. 2nd ed. Cambridge: Cambridge University Press; 1992.
[37] Wang KK, Cohen C, Koch DL, Hieber CA, Yoon K, Gupta M, et al. "Cornell injection molding program progress report", No.16. Cornell University; 1991.
[38] Brandrup J, Immergut EH. Polymer handbook. 3rd ed. New York: Wiley-Inter Science; 1989.